# Metal-insulator-metal plasmon nanocavities: Analysis of optical properties

Yoichi Kurokawa*
*International Center for Young Scientists, National Institute for Materials Science, 1-1 Namiki, Tsukuba, Ibaraki 305-0044, Japan*

Hideki T. Miyazaki
*Quantum Dot Research Center, National Institute for Materials Science, 1-2-1 Sengen, Tsukuba, Ibaraki 305-0047, Japan*
(Received 3 July 2006; revised manuscript received 7 October 2006; published 12 January 2007)

We present detailed analysis of the optical properties of a structure called a nanosheet plasmon cavity. It is a metal-insulator-metal (MIM) waveguide with a finite length. First, propagation of the lowest-energy surface-plasmon mode of a MIM waveguide, which is the fundamental structure of our cavity, is analytically investigated. In addition to the dispersion relation, localization and dissipation of the electromagnetic energy are discussed. Next, the optical properties of the nanosheet plasmon cavity are numerically examined with the boundary element method. The nanosheet plasmon cavity is found to inherit various natures of the original MIM waveguide. The resonance in this cavity can be understood as a Fabry-Perot-like resonance caused by the reflection of the guided mode at the entrance and the exit surfaces. This enables easy design of a cavity on the basis of the analytical dispersion relation of a MIM waveguide. The fields in a MIM waveguide are localized around the dielectric core, and the wavelength of the surface plasmon becomes shorter with decreasing the thickness of the core. Therefore the electromagnetic energy can be confined in a volume as small as 0.001 $\mu m^3$ in a nanosheet plasmon cavity. Another feature of this cavity is that the electric field is maximized at the core entrance. By only letting molecules be adsorbed on the surface of the core, the molecules are exposed to the maximum field. This exhibits great potential of the nanosheet plasmon cavity for enhanced Raman spectroscopy.

DOI: 10.1103/PhysRevB.75.035411 PACS number(s): 78.67.−n, 71.36.+c, 71.45.Gm, 73.20.Mf

## I. INTRODUCTION

A surface plasmon is an electromagnetic wave which couples with free electron plasma bound to an interface between a dielectric and a metal.[1,2] The surface plasmon on rough metal surfaces or in metal nanoparticles results in the localized resonance. Due to the resonance, Raman scattering from adsorbed molecules is drastically enhanced. This phenomenon has been of great interest for more than thirty years.[3] Recently, plasmonics in controlled nanostructures, such as nanohole arrays in metal slabs,[4] nano-optical circuits,[5] and metamaterials,[6] have been of growing interest. Since Raman scattering with single molecule sensitivity was discovered in silver nanoparticle pairs,[7] the plasmon resonance in structures with a small gap has gained particular attention. Various structures have been studied theoretically[8–12] and experimentally.[13–18] However, an issue of reproducible fabrication of a nanometer sized gap was unsolved.

Recently, we proposed a nanosheet plasmon cavity as a solution to the fabrication issue and demonstrated the controlled plasmon resonance in nanometer sized gaps.[19] The nanosheet plasmon cavity is a metal-insulator-metal (MIM) waveguide with a finite length. In this structure, the light energy is confined in the dielectric core, sandwiched between metal layers.[20] The thickness of the core can be reduced to a few nanometers by using a thin-film technique: it is a key point of our cavity. The supported surface plasmon is reflected at the entrance and the exit surfaces of the MIM waveguide. Therefore the Fabry-Perot-like resonance is obtained from a waveguide of a finite length, when the length of the cavity coincides with multiples of half wavelength of the surface plasmon.[21–27] The wavelength of the surface plasmon is shortened if the thickness of the core is decreased.[28] Hence thin and short cavity can be realized. The smallest core that we have fabricated was measured to be 3.3 nm in thickness and 55 nm in length.[19] The shortest surface plasmon polariton wavelength was measured as 51 nm, less than 8% of the free-space wavelength. This corresponds to an extreme ultraviolet wavelength.

Thin-film technique has long been used to fabricate the MIM waveguide for transmission lines[29] and light emitting devices.[30–32] A MIM structure with a nanometer sized dielectric core has been produced for the study of electron tunneling emission.[33,34] In addition, the importance of finite length slits as a nanometer sized cavity has been highlighted.[21–27] However, the combination of two factors, the finite length and the nanometer sized slit fabricated by using the thin-film technique, has not been demonstrated. This architecture not only enables confinement of light in a small volume but also provides another feature; if a molecule is only adsorbed on the dielectric core, we can put the molecule at the maximum field. Thus it is suggested that the nanosheet plasmon cavities are suitable for the application to enhanced Raman spectroscopy.

In this paper, the optical properties of the nanosheet plasmon cavities are discussed in detail, especially from the theoretical viewpoint, because the experimental and the calculated results were limited in the previous paper.[19] A fundamental structure of the nanosheet plasmon cavities is the MIM waveguide. Hence the dispersion relation, the propagation length, and the energy density distribution of the MIM waveguide are outlined in Sec. II. Next, the numerical method for the investigation of the optical properties of the nanosheet plasmon cavities is presented in Sec. III. The fabrication and the observation techniques of the optical prop-

 

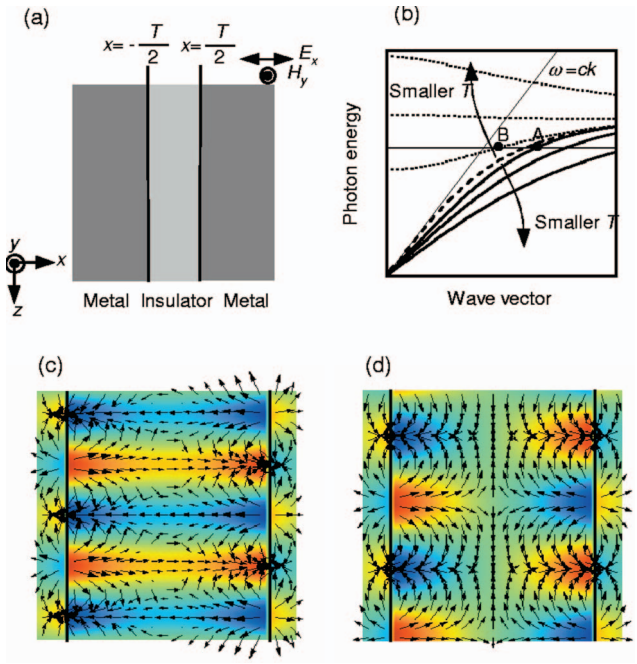


FIG. 1. (Color) (a) A MIM waveguide. The thickness of the core is denoted by $T$. The coordination system and the directions of $E_x$ and $H_y$ are represented. (b) The dispersion relation of the TM mode, which propagates along the $z$ direction of the MIM waveguide made of an ideal Drude metal. The vertical and the horizontal axes mean the photon energy and the wave vector, respectively. The broken line is the dispersion relation for a single interface. The dispersion relation of the MIM waveguide is denoted by the solid and the dotted lines. The mode of the single interface is split into the low-energy mode (solid lines) and the high-energy mode (dotted lines). (c) and (d) The magnitude and the direction of the electric field for the low- and the high-energy modes are denoted by arrows, respectively. The color represents the distribution of $E_x$ in algebraic size. Red shows positive and blue shows negative. (c) and (d) correspond to the points A and B in (b). (c) and (d) explicitly show that the low- and the high-energy modes in (b) are the symmetric and the antisymmetric modes, respectively.

erties are also outlined. In Sec. IV the results are presented. First, the field intensity enhancement is discussed. According to the distribution of the electromagnetic field, the resonance of the nanosheet plasmon cavities is easily understood, based on the picture of the MIM waveguide. Moreover, the far-field reflectance spectra, obtained from the experimental results, are compared with those of the calculated results. The dispersion relation and the energy density of the plasmon modes are also discussed. Through this paper, we employ macroscopic electromagnetics based on continuous materials. Comments on its validity and limitation are added as well. Finally, this study is summarized in Sec. V.

## II. MIM WAVEGUIDE

Here, we will discuss the propagation of an electromagnetic wave along a dielectric core that is sandwiched between metal claddings.[35–37] This configuration is illustrated in Fig. 1. The thickness of the core is denoted by $T$. This core has infinite extent in the $y$ and $z$ directions. $\epsilon_0$ is the dielectric constant of the vacuum. $\epsilon_m(\omega)$ and $\epsilon_i$ are the relative dielectric constants of the metal and the dielectric, respectively, where $\epsilon_m(\omega)$ is dependent on frequency $\omega$.

The eigenequations, which give the dispersion relation of the TM (transverse magnetic) propagation modes, are derived. We deal with the symmetric modes that propagate in the $z$ direction at the wave vector $k$ and frequency $\omega$, i.e., $E_x(\mathbf{r},\omega)$, $E_z(\mathbf{r},\omega)$, $H_y(\mathbf{r},\omega) \propto \exp[i(kz-\omega t)]$. The symmetry is defined with respect to $E_x(\mathbf{r},\omega)$ in this paper.

In $|x| > T/2$,

$$E_x^m(\mathbf{r},\omega) = A \exp(-k_m|x|), \tag{1}$$

$$H_y^m(\mathbf{r},\omega) = A\frac{\omega\epsilon_0\epsilon_m(\omega)}{k} \exp(-k_m|x|), \tag{2}$$

$$E_z^m(\mathbf{r},\omega) = -\frac{ik_m}{k}\frac{|x|}{x}A \exp(-k_m|x|). \tag{3}$$

And, in $|x| < T/2$,

$$E_x^i(\mathbf{r},\omega) = 2B \cosh(k_i x), \tag{4}$$

$$H_y^i(\mathbf{r},\omega) = 2B\frac{\omega\epsilon_0\epsilon_i}{k} \cosh(k_i x), \tag{5}$$

$$E_z^i(\mathbf{r},\omega) = i2B\frac{k_i}{k} \sinh(k_i x), \tag{6}$$

where $k_m = \sqrt{k^2 - \frac{\omega^2}{c^2}\epsilon_m(\omega)}$ and $k_i = \sqrt{k^2 - \frac{\omega^2}{c^2}\epsilon_i}$. $A$ and $B$ are arbitrary constants. The eigenequation is obtained from the boundary condition at the metal-dielectric interface,

$$-\frac{k_m}{k_i} = \frac{\epsilon_m(\omega)}{\epsilon_i} \tanh(k_i T/2). \tag{7}$$

Similarly, the eigenequation of the antisymmetric modes is given by

$$-\frac{k_m}{k_i} = \frac{\epsilon_m(\omega)}{\epsilon_i} \coth(k_i T/2). \tag{8}$$

First, we consider the case of an ideal metal with the Drude property $\left[\epsilon_m(\omega) = 1 - \frac{\omega_p^2}{\omega^2}\right]$, in order to outline the general features of the MIM waveguide. $\omega_p$ is plasma frequency. Figure 1(b) is the dispersion relation of the MIM waveguide. The broken line is the dispersion relation of the single interface case. In the case of the MIM waveguide, the mode of the single interface is split into two modes because of the coupling between the surface plasmon of the two interfaces.[35] This split increases with decreasing $T$ since the coupling between the two interfaces becomes stronger. The $E_x$ distributions of the low-energy mode and the high-energy mode are symmetric and antisymmetric as shown in Figs. 1(c) and 1(d). While the total internal reflection incidence is usually used for momentum-matched excitation of the surface plasmon, it is also possible to excite the surface plasmon by light incident on the end face.[38] The perpendicularly incident plane wave can excite only the low-energy mode be-

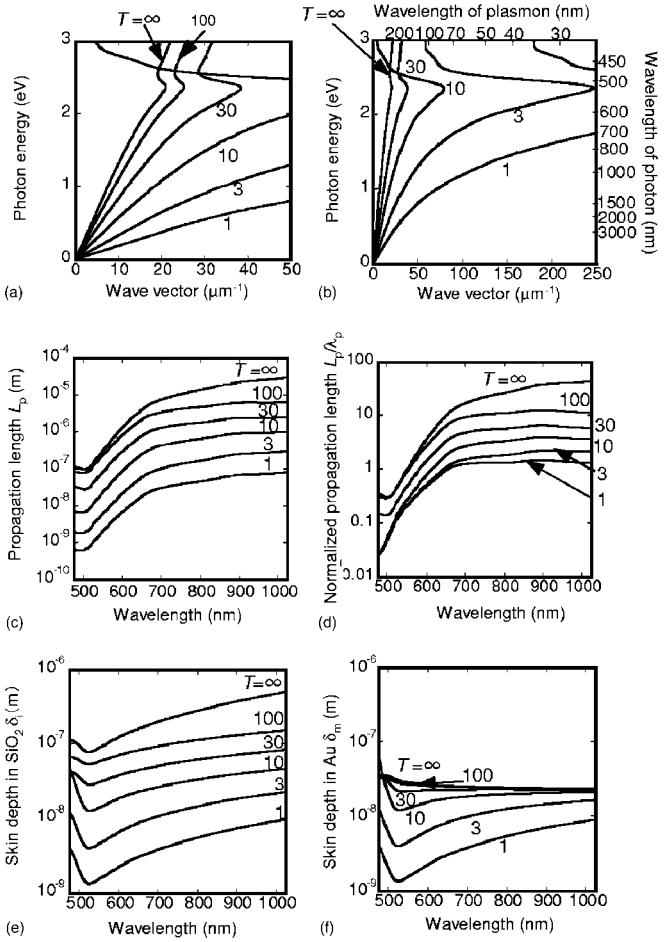


FIG. 2. (a) and (b) The dispersion relation of the TM modes of the MIM waveguide made of Au and $SiO_2$ for various $T$ values. (a) shows enlarged view of small wave-vector region, while (b) shows much wider region. The unit of $T$ is nm. The dispersion for a single interface is denoted by $T=\infty$. The wavelength of the surface plasmon and that of photon are represented in the upper and right sides of (b) for reference. (c) The propagation length of plasmon $L_p$ in the MIM waveguide. (d) The ratio of $L_p$ to $\lambda_p$ in the MIM waveguide. (e) and (f) The skin depths in $SiO_2$ ($\delta_i$) and in Au ($\delta_m$).

cause of the matching of symmetry. Thus we discuss only the symmetric low-energy mode hereafter.

Next, the dispersion relation of the MIM waveguide composed of a realistic material is discussed. The nanosheet plasmon cavity was fabricated by using Au and $SiO_2$ as a metal and a dielectric.[19] We used the reported values[39] and the value of 2.1 for the dielectric constants of Au and $SiO_2$, respectively. Figures 2(a) and 2(b) are the dispersion relation of this waveguide. The dispersion relation becomes flat when $T$ is small, that is, the wavelength of the surface plasmon ($\lambda_p$) becomes shorter. This phenomenon is the same as that illustrated in Fig. 1(b). A major difference between Figs. 1(b) and 2(b) is the turn around the photon energy 2.4 eV in Fig. 2(b).[40] This turn is derived from the imaginary part of the Au dielectric function. Therefore the minimum $\lambda_p$ is a finite value in real structures.

In the case of a real metal, when a surface plasmon propagates along the interface, the intensity decays as a function of $\exp(-2\,\mathrm{Im}[kz])$, due to the energy loss for Joule heat. The propagation length is evaluated by $L_p=|2\,\mathrm{Im}[k]|^{-1}$.[41] Figure 2(c) displays $L_p$ of the MIM waveguide. In every structure, when the wavelength of the incident light ($\lambda$) changes from 1000 to 500 nm, $L_p$ becomes two orders shorter due to the effect of the absorption of Au. In addition, $L_p$ becomes shorter for smaller $T$;[37] the difference between $T=100$ and 1 nm is two orders. If the MIM waveguide is used for signal transmission, $L_p$ itself is important. However, our purpose is the application of this waveguide to cavities. Thus the cycle of the oscillation, i.e., $L_p/\lambda_p$, is more important than $L_p$ itself. $L_p/\lambda_p$ would be a key factor in the determination of the sharpness of resonance (quality factor). $L_p/\lambda_p$ is shown in Fig. 2(d). It is found that the propagation modes of the MIM waveguide decay after a few oscillations. While $L_p/\lambda_p$ again decreases as a function of $T$, this change is smaller than that of $L_p$ itself. The difference of $L_p/\lambda_p$ between $T=100$ and 1 nm is less than one order. In the case of using the waveguide for a cavity, the decrease in the performance that originates from a decreasing $T$ is expected to be small, compared with the case for transmission lines.

Figures 2(e) and 2(f) show the skin depths in the dielectric core ($\delta_i$) and in the metal claddings ($\delta_m$). The skin depths are defined as $\delta_i=(\mathrm{Re}[k_i])^{-1}$ and $\delta_m=(\mathrm{Re}[k_m])^{-1}$. $\delta_i$ of the single interface is a few 100 nm. $\delta_i$ becomes shorter as $T$ decreases. $\delta_i$ at $T=1$ nm is smaller by less than an order of magnitude than that of the single interface. In contrast, $\delta_m$ of even a single interface is about 25 nm. The reduction of $\delta_m$ for a decreasing $T$ is small, compared with that of $\delta_i$. In the case of the MIM waveguide, the electromagnetic energy can be confined in a dielectric core,[20,37] since $\delta_m$ is smaller than $\delta_i$.

While the localization of the energy in a very thin volume around the core has been discussed from the viewpoint of the electric power flow in Ref. 20, in our study it is discussed from the energy density distributions.[37,42] The electric and magnetic energy densities in the dielectric core ($u_e^i$ and $u_m^i$) are

$$u_e^i(x,\omega)=\frac{1}{4}\epsilon_0\epsilon_i|\mathbf{E}^i(x,\omega)|^2=\frac{1}{4}\epsilon_0\epsilon_i\left|\frac{\epsilon_m(\omega)}{\epsilon_i}\frac{\exp(-k_mT/2)}{\cosh(k_iT/2)}\right|^2|A|^2\times\left(|\cosh(k_ix)|^2+\left|\frac{k_i}{k}\sinh(k_ix)\right|^2\right),\tag{9}$$

$$u_m^i(x,\omega)=\frac{\epsilon_0}{4}\left|\frac{\omega\epsilon_m(\omega)}{ck}\frac{\exp(-k_mT/2)}{\cosh(k_iT/2)}\right|^2|A\cosh(k_ix)|^2.\tag{10}$$

The energy density in the metal is obtained from the Poynting theorem of dispersive media.[43] The electric and magnetic energy densities ($u_e^m$ and $u_m^m$) are thus

$$u_e^m(x,\omega)=\frac{\epsilon_0}{4}\mathrm{Re}\left(\frac{\partial\{\omega\epsilon_m(\omega)\}}{\partial\omega}\right)|\mathbf{E}^m(x,\omega)|^2=\frac{\epsilon_0}{4}\mathrm{Re}\left(\frac{\partial\{\omega\epsilon_m(\omega)\}}{\partial\omega}\right)|A\exp(-k_m|x|)|^2\times\left(1+\left|\frac{k_m}{k}\right|^2\right),\tag{11}$$

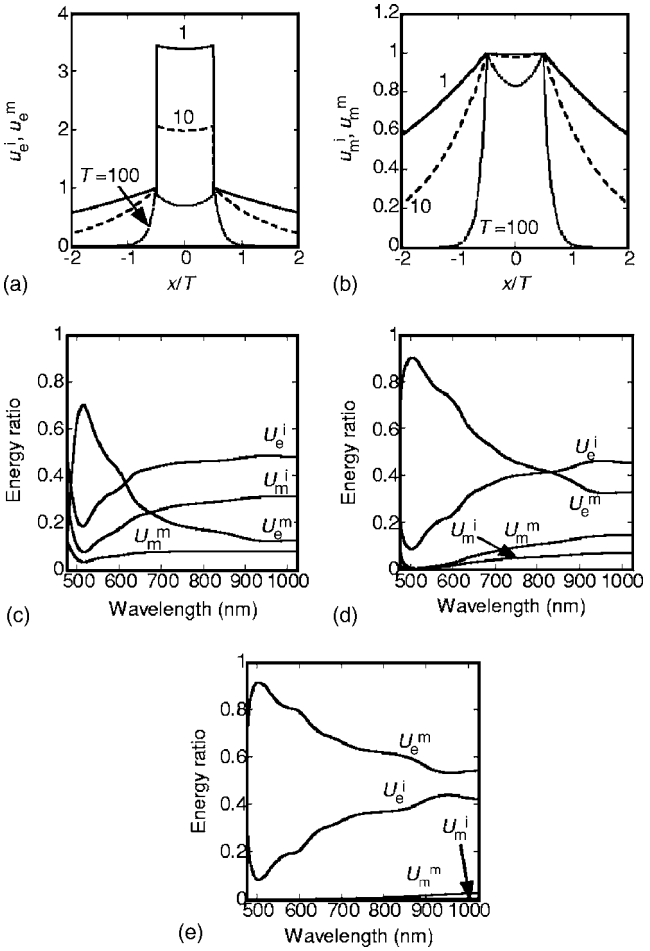


FIG. 3. (a) The electric and (b) the magnetic energy density profiles along the $x$ cross section of the MIM waveguides made of Au and $SiO_2$ for $\lambda=800$ nm. The horizontal axes are $x$ normalized by $T$. The vertical axes are adjusted so that the energy densities at the metal side of the interfaces equal each other. (c)–(e) Ratio of the electric and magnetic energy localized in the metal (Au) and the dielectric ($SiO_2$) to the whole energy in the MIM waveguide. (c) $T=100$ nm, (d) $T=10$ nm, and (e) $T=1$ nm.

$$u_m^m(x,\omega)=\frac{\epsilon_0}{4}\left|A\frac{\omega\epsilon_m(\omega)}{ck}\exp(-k_m|x|)\right|^2. \tag{12}$$

The energy density profiles in the $x$ direction for several $T$ values at a typical wavelength $\lambda=800$ nm are presented in Figs. 3(a) and 3(b). The horizontal axes are normalized by $T$. The vertical axes are adjusted so that the energy densities at the metal side of the metal-dielectric interfaces equal each other. It is found that the energy density is high in the dielectric core and shows the maximum at the metal-dielectric interface for every $T$. For a smaller $T$, the leakage of energy into the metal claddings increases significantly, and the ratio of the energy in the core becomes lower. This is because $\delta_m$ hardly changes.

In order to discuss the detail of this behavior, the ratio between the energy in the dielectric core and that in the metal claddings is investigated. Total energy in each region is calculated by integrating the energy density Eqs. (9)–(12),

$$\begin{aligned}U_e^i&=2\int_0^{T/2}u_e^i(x,\omega)dx\\&=\frac{\epsilon_0}{8\epsilon_i}\left|\epsilon_m(\omega)\frac{\exp(-k_mT/2)}{\cosh(k_iT/2)}\right|^2|A|^2\\&\times\left[\frac{\sinh(\mathrm{Re}[k_i]T)}{\mathrm{Re}[k_i]}\left(1+\left|\frac{k_i}{k}\right|^2\right)\right.\\&\left.+\frac{\sin(\mathrm{Im}[k_i]T)}{\mathrm{Im}[k_i]}\left(1-\left|\frac{k_i}{k}\right|^2\right)\right],\end{aligned} \tag{13}$$

$$\begin{aligned}U_m^i&=2\int_0^{T/2}u_m^i(x,\omega)dx\\&=\frac{\epsilon_0}{8}\left|\frac{\omega\epsilon_m(\omega)}{ck}\right|^2|A|^2\left|\frac{\exp(-k_mT/2)}{\cosh(k_iT/2)}\right|^2\\&\times\left(\frac{\sinh(\mathrm{Re}[k_i]T)}{\mathrm{Re}[k_i]}+\frac{\sin(\mathrm{Im}[k_i]T)}{\mathrm{Im}[k_i]}\right),\end{aligned} \tag{14}$$

$$\begin{aligned}U_e^m&=2\int_{T/2}^{\infty}u_e^m(x,\omega)dx\\&=\frac{\epsilon_0}{4}\left(1+\left|\frac{k_m}{k}\right|^2\right)|A|^2\mathrm{Re}\left(\frac{\partial\{\omega\epsilon_m(\omega)\}}{\partial\omega}\right)\\&\times\frac{\exp(-\mathrm{Re}[k_m]T)}{\mathrm{Re}[k_m]},\end{aligned} \tag{15}$$

$$U_m^m=2\int_{T/2}^{\infty}u_m^m(x,\omega)dx=\frac{\epsilon_0}{4}\left|A\frac{\omega\epsilon_m(\omega)}{ck}\right|^2\frac{\exp(-\mathrm{Re}[k_m]T)}{\mathrm{Re}[k_m]}. \tag{16}$$

The energy ratio of each component, with $A$ chosen so $U_e^i+U_m^i+U_e^m+U_m^m=1$, for several $T$ values is shown in Figs. 3(c)–3(e). For $T=100$ nm, most of the energy is stored in the dielectric core in the form of the electric energy. The ratio of $U_e^i$ does not change significantly for a wide range of $T$. However, when $T$ gets smaller, the ratio of $U_e^m$ becomes drastically higher. When $T\leqslant 10$ nm, $U_e^m$ exceeds $U_e^i$. For $T=1$ nm, most of the energy is localized in the metal claddings as electric energy. As $T$ decreases, $U_m^i$ and $U_m^m$ get lower; they are vanishingly small at $T=1$ nm. A reduction of $L_p$ and an increase of the energy loss for a decreasing $T$ are attributed to the growth of $U_e^m$. However, confinement of a considerable amount of the electric energy in the dielectric ($U_e^i$) for $T=1$ nm is noteworthy.

## III. CALCULATION AND EXPERIMENT

In this section calculation and experimental methods are outlined for discussing the optical properties of nanosheet plasmon cavities.

### A. Calculation

Because the nanosheet plasmon cavity is a MIM waveguide with a finite length, the discussion of the previous

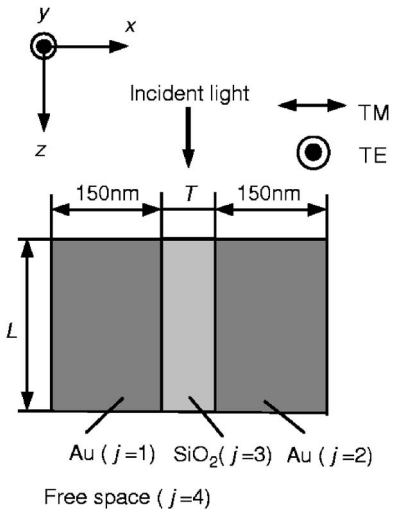


FIG. 4. The calculation model of a nanosheet plasmon cavity. It is a 2D model uniform in the $y$ direction. The thickness and the length of the core are denoted by $T$ and $L$, respectively. Light is incident downward from the upper side of the cavity. The directions of the electric field for TM and TE modes are shown.

section is insufficient. A numerical examination is necessary to investigate the optical properties of this cavity. We employ the boundary element method (BEM).[44] The BEM is suitable for modeling the nanosheet plasmon cavities, which have a few 100-nm widths and a few nm-sized gap, since the size of each element can be chosen arbitrary. Moreover, treatment of an open system is easy, and there is no limitation on the dielectric function.

The calculation model, which represents a nanosheet plasmon cavity, is illustrated in Fig. 4. In this study, we consider standing waves of only one direction ($z$ direction) for simplicity. Therefore we constructed a two-dimensional (2D) model. The length of the core is denoted by $L$. $T$ continues to show the thickness of the core. The width of the Au claddings was set to 150 nm. This structure is assumed to be uniform in the $y$ direction. The corners are rounded off at a radius $R_c$=0.25 nm,[45] which will be discussed in detail in Appendix A. The regions of the two Au claddings, the $SiO_2$ core, and free space are marked by $j$=1, 2, 3, and 4, respectively. Light is incident from the upper side of the structure to $+z$ direction. In the 2D system, the transverse magnetic (TM) modes ($H_x$=$H_z$=$E_y$=0) and the transverse electric (TE) modes ($E_x$=$E_z$=$H_y$=0) can be treated separately.

In each polarization, the electromagnetic field is expressed by the 2D Helmhotz equations in each region,

$$(\nabla^2 + k_j^2)\Psi_j(\mathbf{r}) = 0. \tag{17}$$

$\Psi(\mathbf{r})$ is $H_y$(TM) or $E_y$(TE), and $k_j$ is the wave number in each region. The solution of Eq. (17) can be obtained as a boundary integral equation,[27,44]

$$\Psi_j(\mathbf{r}) = \oint_{c_j} \left[ G_j(\mathbf{r},\mathbf{r}') \frac{\partial \Psi_j(\mathbf{r}')}{\partial \mathbf{n}'} - \Psi_j(\mathbf{r}') \frac{\partial G_j(\mathbf{r},\mathbf{r}')}{\partial \mathbf{n}'} \right] d\mathbf{r}'. \tag{18}$$

Here, $\mathbf{n}$ is an outgoing normal vector, and the Green's function $G_j(\mathbf{r},\mathbf{r}')$ is given by

$$G_j(\mathbf{r},\mathbf{r}') = \frac{i}{4} H_0^{(1)}(k_j|\mathbf{r}-\mathbf{r}'|), \tag{19}$$

where $H_0^{(1)}(k_j|\mathbf{r}-\mathbf{r}'|)$ is the 0th order of the first kind of Hankel function.

To obtain the electromagnetic field from Eq. (18), the electromagnetic field and its normal derivative on the boundary are required. Thus the boundary is divided into elements, and observation point $\mathbf{r}$ of Eq. (18) is approximated to each element. Then, the system of equations

$$\mathbf{A}\vec{\mathbf{b}} = \vec{\mathbf{c}} \tag{20}$$

is obtained, where $\mathbf{A}$ is a matrix that shows the structure of the cavity, $\vec{\mathbf{b}}$ is a vector that represents the internal or the scattered field on the boundary, and $\vec{\mathbf{c}}$ is a vector that reflects the incident field. After $\vec{\mathbf{b}}$ is obtained, $H_y$ (TM) and $E_y$ (TE) can be calculated from Eq. (18). $E_x$ and $E_z$ of the TM modes, and $H_x$ and $H_z$ of the TE modes are obtained from Maxwell's equations.

### B. Experiment

The special feature of our nanosheet plasmon cavity is the employment of a thin-film technique for the fabrication of a slit sandwiched between metal claddings; rather than of patterning techniques such as electron-beam lithography followed by etching,[14–17] focused ion beam (FIB),[18] and soft lithography.[46] While reproducible realization of a slit narrower than 10 nm by using current patterning techniques is difficult,[16,17] deposition of a nm-thick thin film is sufficiently feasible with established techniques.

$Au/SiO_2/Au$ multilayers were coated on fused silica substrates by dc/rf magnetron sputtering deposition. The thickness of the Au layers was 150 nm, which is sufficiently thicker than $\delta_m$. This value was chosen to avoid any effect of the fused silica substrate. $T$ of the $SiO_2$ layer was 56, 14, and 3.3 nm. Transmission electron microscopy (TEM) was used to measure $T$ and to inspect the morphology of $SiO_2$ films. The cross section of the multilayer for $T$=3.3 nm is represented in Fig. 5(a). The sharpness of the $Au/SiO_2$ interfaces, and the continuity and the thickness uniformity of the $SiO_2$ film can be confirmed. The $SiO_2$ films are wavy due to the surface roughness of the first Au layer. Although excessive scattering of surface plasmons by such undulations was anticipated, no explicit effects on the optical properties were revealed in this study. While a 5-nm-thick Cr film was inserted as an adhesion layer between the fused silica substrate and the first Au layer, the $SiO_2$ core and the Au claddings are in direct contact with each other without any intermediate layer; this is because these interfaces are of prime importance for surface plasmons.

A nanosheet plasmon cavity is a MIM waveguide cut out to a finite length $L$. To form the standing wave, $L$ should be comparable with $\lambda_p$; i.e., necessary $L$ falls within a range from several 10 nm to several 100 nm based on the upper axis of Fig. 2(b). Such relatively large features are sufficiently realizable by using conventional patterning techniques. We milled the $Au/SiO_2/Au$ multilayers from the nor-

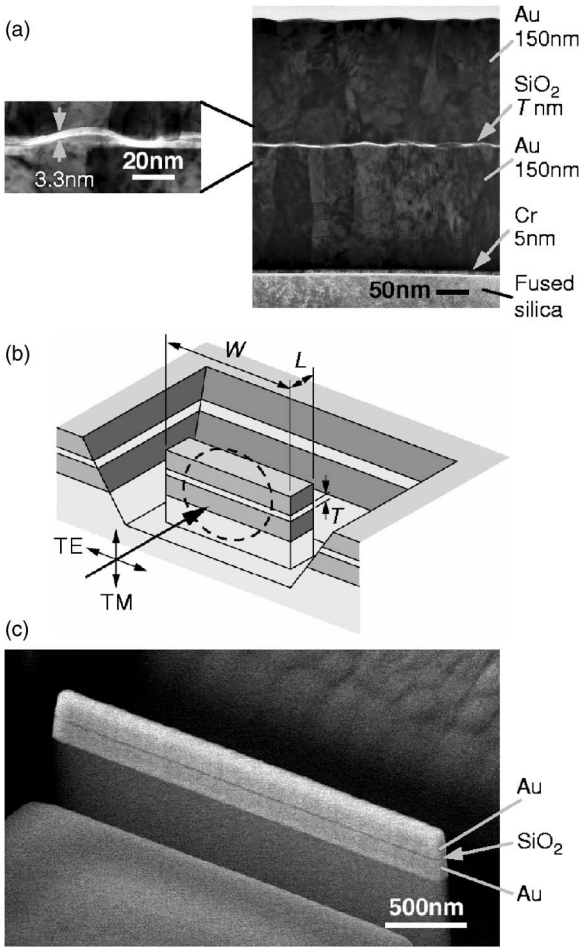


FIG. 5. (a) TEM micrograph of the cross section of a $Au/SiO_2/Au$ multilayer for $T=3.3$ nm. Magnified image of the $SiO_2$ film is shown on the left. The $SiO_2$ film looks duplicated, because the film is undulated within the finite thickness of the TEM specimen and the vicinities of convex and concave points of the film look brighter. (b) Schematic drawing of a cavity after FIB milling. Rectangular cavities with a width of $W$ and a length of $L$ were fabricated by removing the surroundings. The walls facing the cavity are not perpendicular to the substrate but slanted. The backscattered light from the area within the circle was measured. (c) Scanning electron micrograph of a fabricated nanosheet plasmon cavity of $T=14$ nm, $L=107$ nm, and $W=3$ $\mu$m.

mal direction with a FIB, and removed the surrounding regions so that rectangular cavities with a width of $W$ and a length of $L$ are left unmilled as shown in Figs. 5(b) and 5(c). For each $T$ value, about 20–30 cavities with different $L$ values ($L=55-483$ nm) were arrayed along one of the edges of the substrate, so that the optical properties can be measured from the side. To minimize the discrepancy between the three-dimensional experimental samples and the 2D theoretical models, $W$ was set at 3 $\mu$m, which is sufficiently long compared with $\lambda_p$. The surrounding walls opposing to the cavities are slanted as illustrated in Fig. 5(b) to prevent unexpected standing waves between the cavity surfaces and the walls. To avoid the redeposition of Au onto the cavity surfaces by FIB milling, the milling process was divided into many steps and the entrance surfaces were finished at the final step. The fabricated length $L$ were measured with a calibrated field-emission scanning electron microscope with an accuracy of ±5 nm. The measurement of $L$ was done after the optical characterization, because the electron beam irradiation could affect the optical properties.[15,17]

The plasmon resonance in a nanostructure can be probed with far-field signals, such as scattering, reflection, transmission, and absorption.[10,12–15,17] In this study, the backscattering spectra of individual cavities were measured. A nearly collimated white light with linear polarization (convergence: ±4.6°) is normally incident on the cavity entrance, and the backscattered light (angular distribution: ±33.4°) was collected with an objective lens. While the entire entrance surface of the cavity was illuminated with the white light, the scattered light only from a selected area [diameter: 2 $\mu$m, Fig. 5(b)] around the center of a single cavity was led to a spectrometer. Though the measurement area also covered the surface of the fused silica substrate, the scattering from the cavity was dominant in each measured signal. The spectra were normalized by that for a Ag mirror. Such a normalized backscattering signal is hereafter simply called reflectance. Reflection for both TM and TE incidence were measured for each cavity.

## IV. RESULTS AND DISCUSSIONS

### A. Electromagnetic fields

The nanosheet plasmon cavity is expected to have good potential for the application to enhanced Raman scattering from molecules placed at the core entrance. Hence the resonance of this cavity is investigated from the field intensity enhancement at the center of the core entrance. Figure 6 represents the field intensity enhancement spectra of each cavity. $T$ is 56, 14, and 3.3 nm corresponding to the size of the fabricated samples. The upper side in Fig. 6 shows the spectra for longer $L$. Clear peaks are found in each spectrum when TM polarized light is incident on the cavity. Peaks shift to longer λ for longer $L$. When $L$ increases more, a new series of peaks appears. It is considered that each series corresponds to a different order resonance as assigned in Fig. 6 (resonance order number is denoted by $m$ hereafter). When $T$ decreases, the field intensity enhancement increases. In the structure for every $T$, the enhancement is lower at shorter λ. The peaks of the higher-order resonances are clear for $T=56$ and 14 nm. However, enhancement at the higher-order resonances is small for $T=3.3$ nm. These behaviors would be derived from a smaller $L_p/\lambda_p$ in Fig. 2(d). The quality factor of each mode is 10–20. In contrast, clear peaks, which are dependent on $L$, cannot be found for TE polarized light [Fig. 6(d)]. In a thicker core, TE guided modes can also propagate.[37] However, all TE modes have a finite cutoff unlike the TM mode in Fig. 2(b). Since the core thickness of our cavities is sufficiently small, TE modes cannot resonate.

It is suggested that these resonances originate from Fabry-Perot-like resonances. To confirm this, the electromagnetic field distributions are investigated. Typical $E_x$ and $H_y$ distributions for peaks of $m=1$, 2, and 3 are presented in Figs. 7(a)–7(f). The standing waves occur at each peak in Fig. 6 as expected. The electric field is localized in the core and is the

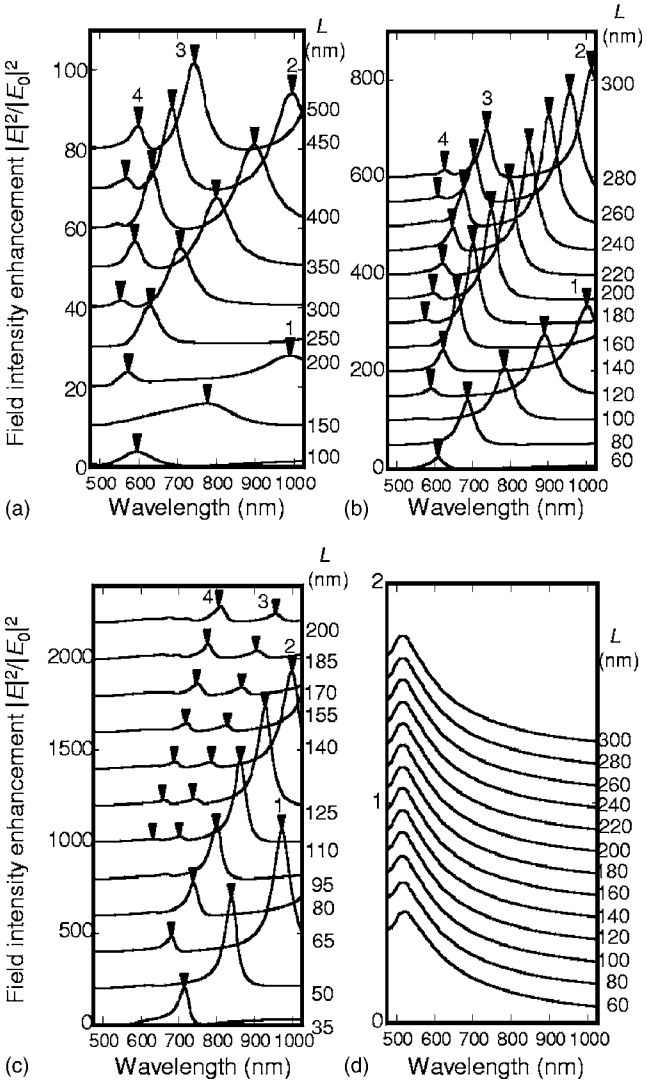


FIG. 6. The field-enhancement spectra at the core entrance. Each spectrum is offset and arranged so that higher spectra correspond to longer $L$. The observation point is put at $x=0$ at the core entrance. The field enhancement is defined as the intensity $|E|^2$ normalized by the incident field intensity $|E_0|^2$. The TM mode for (a) $T=56$ nm, (b) $T=14$ nm, (c) $T=3.3$ nm, and (d) the TE mode for $T=14$ nm. Arrows in (a)–(c) show peak positions. The numbers in (a)–(c) indicate the series of the peaks. They will be confirmed to represent the order numbers of the Fabry-Perot-like resonance from the field distributions in Fig. 7.

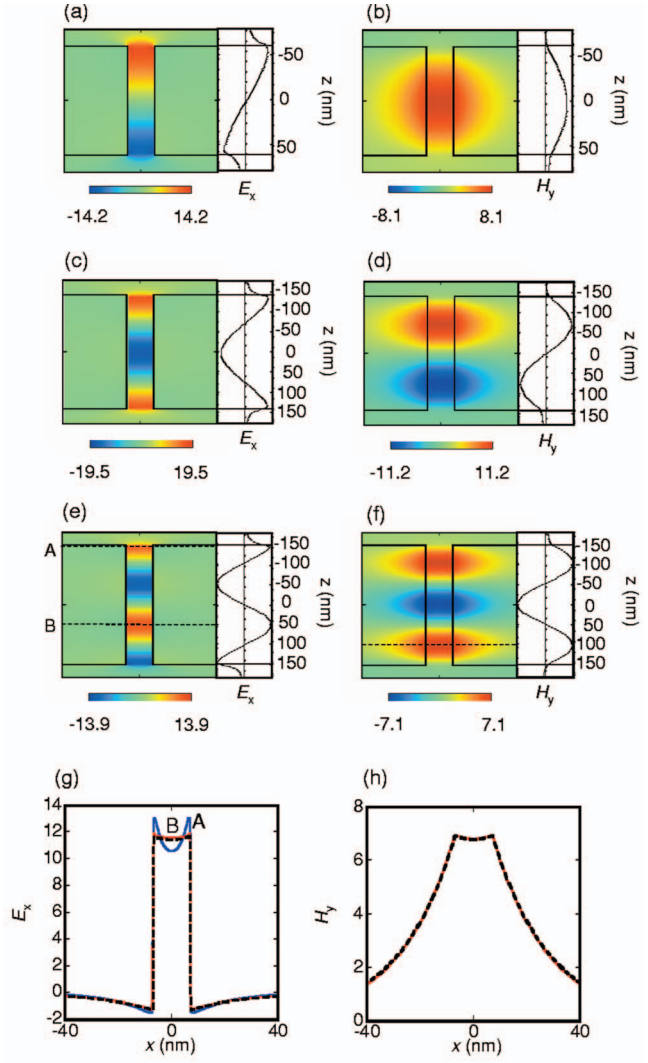


FIG. 7. (Color) Distributions of $E_x$ [(a), (c), and (e)] and $H_y$ [(b), (d), and (f)] in the nanosheet plasmon cavity at typical field-enhancement peaks for $T=14$ nm. (a) and (b) $m=1$ for $L=120$ nm ($\lambda=890$ nm), (c) and (d) $m=2$ for $L=280$ nm ($\lambda=956$ nm), and (e) and (f) $m=3$ for $L=300$ nm ($\lambda=736$ nm). The field profiles on the $z$ axis are also displayed on the right of each panel; the standing-wave nature can be clearly confirmed. (g) The $E_x$ profiles (blue and red) on the lines A and B in (e), respectively, and the analytical $E_x$ profile (dotted line) of the MIM waveguide obtained from Eqs. (1) and (4). (h) The $H_y$ profile (red) on the line in (f), and the analytical $H_y$ profile (dotted line) of the MIM waveguide obtained from Eqs. (2) and (5). Arbitrary constants $A$ and $B$ in Eqs. (1), (2), (4), and (5) were adjusted so that the magnitude of $H_y$ of the MIM waveguide and that of the nanosheet plasmon cavity at $x=0$ coincide with each other. In (g) and (h), the red solid lines and the black broken lines almost overlap.

highest at both ends. The maxima of the electric fields at the both ends can be understood in terms of large effective refractive index of a MIM waveguide.[19,22] When light is incident on an interface from the larger index side, the phase of the reflected wave does not change; i.e., this interface functions as a free end. Consequently, the maxima of the electric fields are located at the both ends. In addition, we found that the area where the electric field leaks out to the free space from the core surfaces is as large as $T$. Therefore a molecule adsorbed on the core entrance can be exposed to a maximum electric field. This feature is important for enhanced Raman spectroscopy. In the structure for $T=3.3$ nm, the maximum electric-field intensity enhancement is $10^3$. This leads to Raman enhancement of $10^6$. In contrast, the magnetic field is highest at the nodes of the electric field, and spreads into the metal.

Figures 7(g) and 7(h) show the electromagnetic field profiles of the nanosheet plasmon cavity and compare them with those of the MIM waveguide obtained from Eqs. (1)–(6). The field profiles of the nanosheet plasmon cavity were cal-

culated for the positions denoted by the dotted lines in Figs. 7(e) and 7(f). The electric field around the entrance side does not agree with those of the MIM waveguide. However, the electric-field profile inside the cavity (the broken line B) and the magnetic-field profile correspond well with that of the MIM waveguide. Thus except at the entrance and the exit ends, the electromagnetic fields in the nanosheet plasmon cavities can be precisely expressed by the analytical solutions of the MIM waveguide.

### B. Reflection spectra

Here, the reflection spectra are discussed to compare the calculated results with the experimental ones. The calculated reflection spectra are defined as a differential scattering cross section for the backward direction ($-z$ direction). The extent of the scattered angle is not included. Figures 8(a)–8(d) are the calculated reflection spectra for various $T$. $L$ increases for the upper side of each panel. Many dips can be found for TM polarized incidence. When $L$ becomes shorter, these dips shift systematically to shorter $\lambda$. Most of the reflection dip positions correspond to peak positions of the field intensity enhancement spectra in Fig. 6. Therefore if reflection spectra are observed, the resonance wavelength can be found from the reflection dips. In contrast, dips cannot be found for TE polarized light. It is equivalent to the absence of the peaks in the field-enhancement spectra of Fig. 6(d). However, even for the TM polarization, reflection dips do not indicate all resonances. For example, there are no signs of resonances of $m=1$ and 2 in the reflection spectra for $T=56$ nm. In addition, the reflection dips for modes of $m=3$ or higher for $T=3.3$ nm are almost indiscernible. The relationship between $L$ and the resonance wavelength is plotted in Figs. 8(e)–8(g). ● and ▲ display the electric-field enhancement peaks in Fig. 6 and the reflection dips in Fig. 7, respectively. The dotted curves are obtained by assuming exact correspondence of the entrance and the exit ends of the cavity with antinodes of the electric field, i.e., $\frac{m}{2}\lambda_p=L$. $\frac{m}{2}\lambda_p=L$ holds for higher modes, but it does not hold for lower modes. Presumably, this is because the entrance and the exit ends do not exactly correspond to the antinodes of the standing wave.

Figure 9 is the experimental reflection spectra. In the case of TM polarized light, there are some dips shifting systematically. On the contrary, systematic dips are not seen for TE polarized light [Fig. 9(d)]. While agreement between the experimental results and the calculated ones is fairly good, there are some discrepancies. Even dips, not predicted in the calculated results, can be found in the experimental results; for example, the modes of $m=2$ for $T=56$ nm, and $m=4$ for $T=3.3$ nm. Some of these dips can be explained by the expansion of the scattering angle. While scattered light of a wider angular range is integrated in the experimental reflection spectra, the extent of the scattering angle is not taken into account in the calculated results in Fig. 8. For example, the experimental reflection dip at $\lambda=728$ nm for $T=56$ nm and $L=280$ nm is not found in the calculated reflection for the perpendicular direction. Nonetheless, this dip is reproduced in the calculation for larger scattering angles [Fig. 10(a)]. Other experimental dips [$m=4$ in Fig. 10(b)] can be explained in the same way. However, some dips cannot be understood from only the scattering angle. For example, the dip presumed to be the resonance of $m=5$ in Fig. 10(b) cannot be explained as just described; and periodic dips, found especially for larger $T$ and smaller $L$ [the curves in Fig. 9(a)], cannot be identified in the calculated results. The former suggests the presence of some additional loss. This will be discussed later. One reason for the latter is considered to be the difference between the calculation model and the experimental sample. While the calculation model is a 2D system, the experimental sample has a finite depth ($y$ direction) where $W=3$ $\mu$m; there could be some resonances also in the $y$ direction.

### C. Dispersion relation of the surface plasmon

$L$ closely corresponds to $m\lambda_p/2$ at the $m$th resonance as shown in Figs. 8(e)–8(g). Thus the wave vector of the surface plasmon is expressed by $k=2\pi/\lambda_p \simeq m\pi/L$. Therefore the dispersion relation of the surface plasmon can be approximately obtained from the resonances of the cavity.[47] Figure 11(a) is the dispersion relation obtained from the calculated field-enhancement peaks in Fig. 6. The dispersion curves experimentally observed from the reflection dips are displayed in Fig. 11(b). The $m$th resonances for various $L$ exhibit unique curves for each $T$. The analytical dispersion relations of the MIM waveguide are also presented in Fig. 11. Good agreement between the dots and the analytical curves suggests that the nanosheet plasmon cavity can be precisely designed on the basis of the dispersion relation of the MIM waveguide. Moreover, from the agreement between the calculated results and experimental ones for $T=3.3$ nm we can find another important thing. For even such a thin film, the solution of Maxwell's equations based on the dielectric function of bulk material, which ignores spatial dispersion and atomic structures, can be applied. The observed minimum $\lambda_p$ is 51 nm ($k=123$ $\mu$m$^{-1}$). This value is obtained from the resonance of $m=3$ at $\lambda=651$ nm in the cavity for $T=3.3$ nm and $L=76$ nm. It is the shortest $\lambda_p$ of any surface plasmon recorded thus far by optical measurement, to our knowledge. However, there is an unignorable disagreement between the calculated results and the experimental ones for $T=14$ nm [Fig. 11(b)]. This disagreement would originate from inaccuracy of the $SiO_2$ film thickness measured by using TEM. One possible reason is the incorrectness of the scale of the TEM. Other reasons could be the fluctuation of the $SiO_2$ film thickness for each substrate, since different substrates, simultaneously deposited, were used for the fabrication of the cavities and for the observation of the film thickness. For reference, the analytical dispersion relation of the MIM waveguide for $T=10$ nm is also presented in Fig. 11(b). It agrees better with the experimental results. It indicates that the true thickness of $SiO_2$ film might be close to 10 nm.

### D. Energy density distribution

It was found that the electromagnetic field is localized in a very thin region around the core from Fig. 7. $L$ is also short, compared with $\lambda$. Here the energy density is discussed

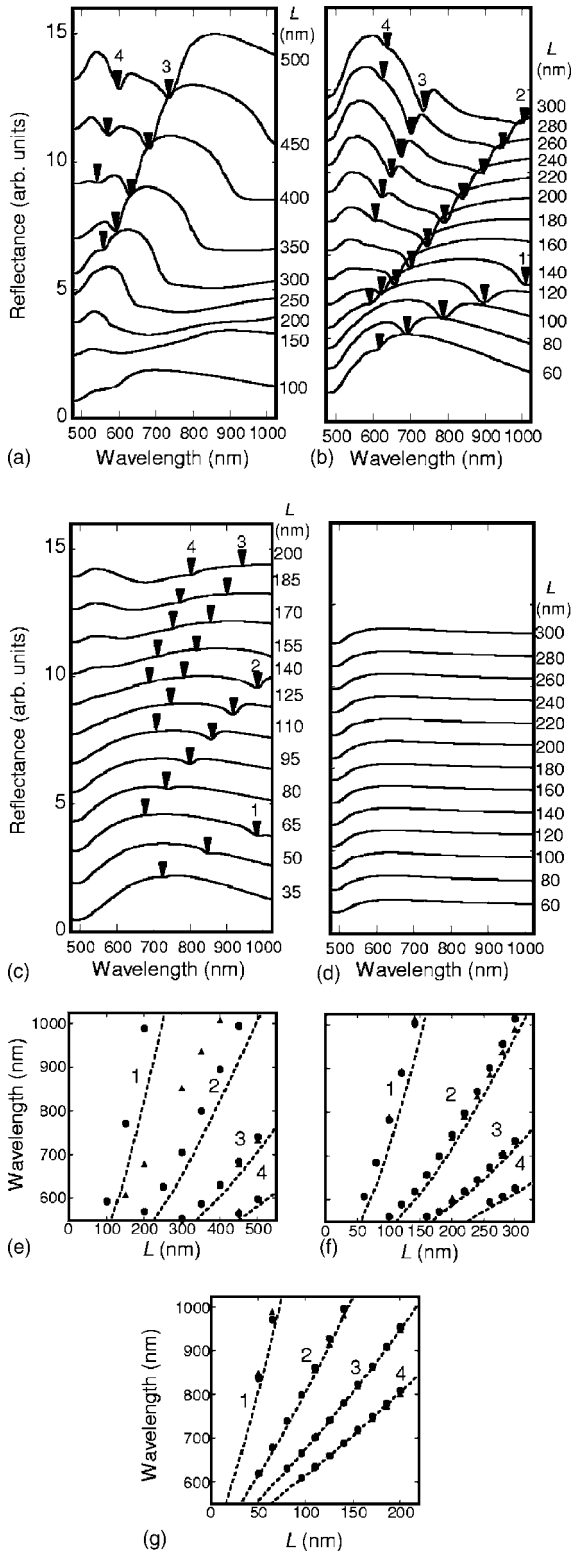


FIG. 8. (a)–(d) The calculated reflection spectra. The TM mode for (a) $T=56$ nm, (b) $T=14$ nm, (c) $T=3.3$ nm, and (d) the TE mode for $T=14$ nm. Each spectrum is offset and arranged so that upper spectrum corresponds to longer $L$. Arrows in (a)–(c) show the dip positions. (e)–(g) The relationship between $L$ and the peak positions in Figs. 6(a)–6(c) (●), and the dip positions in Figs. 8(a)–8(c) (▲). (e) $T=56$ nm, (f) $T=14$ nm, and (g) $T=3.3$ nm. The numbers in (a)–(c) and (e)–(f) are the resonance orders.

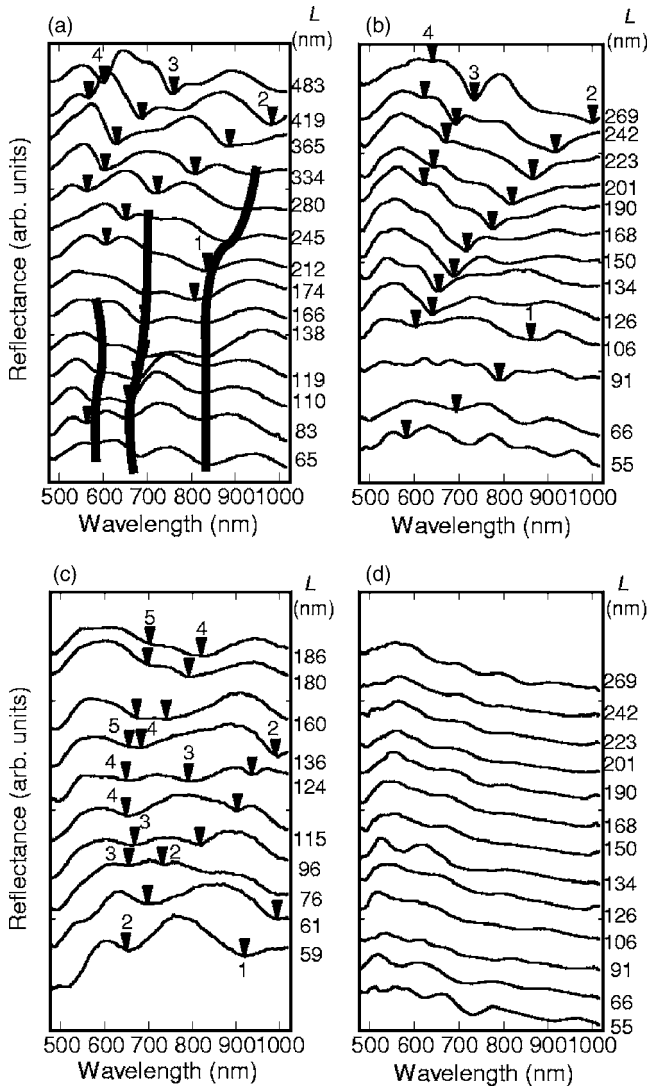


FIG. 9. The experimental reflection spectra. The TM mode for (a) $T=56$ nm, (b) $T=14$ nm, (c) $T=3.3$ nm, and (d) the TE mode for $T=14$ nm. Arrows in (a)–(c) show the major dips, which can be assigned as the resonance. The numbers denote the resonance orders. The gray curves in (a) show the systematic behavior of additional dips which become significant for larger $T$ and smaller $L$.

to calculate how large is the volume in which the electromagnetic energy is confined. Figure 12 is the energy density around the dielectric core for $T=3.3$ nm at typical $m=1$ resonance. The electric energy in Fig. 12(a) is high at the entrance and the exit ends. In contrast, the magnetic energy in Fig. 12(b) shows the maximum at the central part of the core and spreads into the metal claddings. Figure 12(c) is the total-energy density. The total energy is dominated by the electric energy; the maximum energy is obtained at the entrance and the exit ends. Moreover, confinement of the energy in the dielectric core is clearly found.

Finally, the mode volume ($V_{mod}$) of our cavity is discussed. From Fig. 12, it is found that the size of the region outside the cavity into which significant energy has leaked is small. While the leaked energy in the third direction ($y$ direction) cannot be calculated by our 2D model, it is also

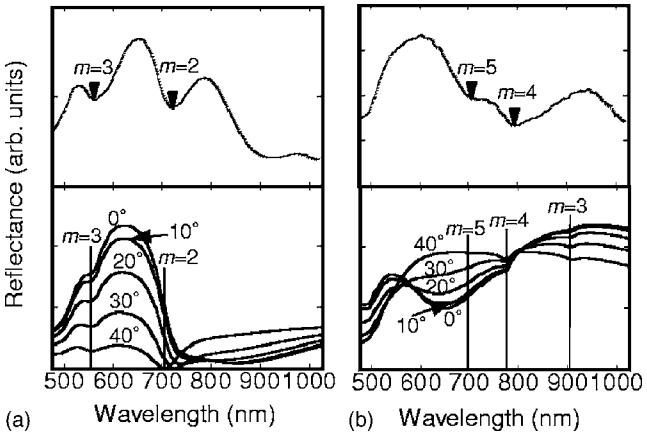


FIG. 10. (a) Upper, the experimental reflection spectra for $T=56$ nm and $L=280$ nm, and lower, the calculated reflection spectra for $T=56$ nm and $L=300$ nm for various scattering angles. A dip, which is supposed to correspond to the resonance of $m=2$, is observed at $\lambda=728$ nm in the experimental result. On the other hand, such a dip cannot be found in the calculated result for 0°. However, a dip corresponding to the resonance of $m=2$ is present in the calculated result for larger scattering angles. The dip for $m=2$ in the experimental result would originate from such large angle components. (b) Upper, the experimental reflection spectra for $T=3.3$ nm and $L=180$ nm, and lower, the calculated reflection spectra for $T=3.3$ nm and $L=185$ nm. While the dip of $m=4$ can also be explained by the large extent of the scattering angle, that of $m=5$ cannot. In the calculation results, field-enhancement peak positions are also indicated with vertical lines. Absence of a dip for $m=3$ in the experiment in (b) would be reasonable, because the dip in the calculation is small for all scattering angles.

expected to be similarly low. In comparison with such leaked energy region, $W=3$ $\mu$m is much longer. Therefore energy leakage in the $y$ direction can be ignored in this study, i.e., $V_{mod}$ is obtained from the multiplication of the mode area (the mode volume per unit length) based on 2D calculation and $W$. $V_{mod}$ is defined by[48]

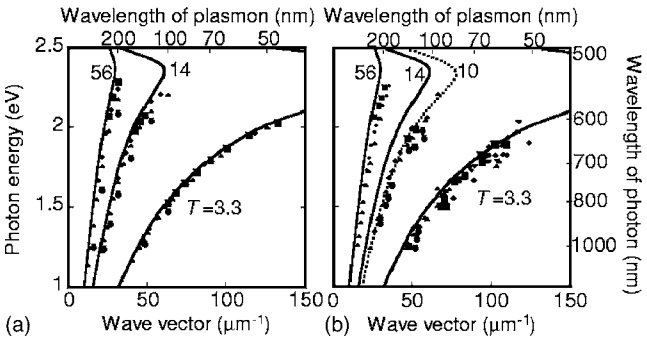


FIG. 11. (a) and (b) The dispersion relation obtained from the calculated field-enhancement peaks in Fig. 6 and the experimental reflection dips in Fig. 9, respectively. The solid curves are the analytical dispersion relations of the MIM waveguide. The unit of $T$ is nm. ●, ▲, ◆, ■, and ▼ are the resonance of $m=1$, 2, 3, 4, and 5. The broken curve in (b) is the dispersion relation for the MIM waveguide of $T=10$ nm shown for reference.

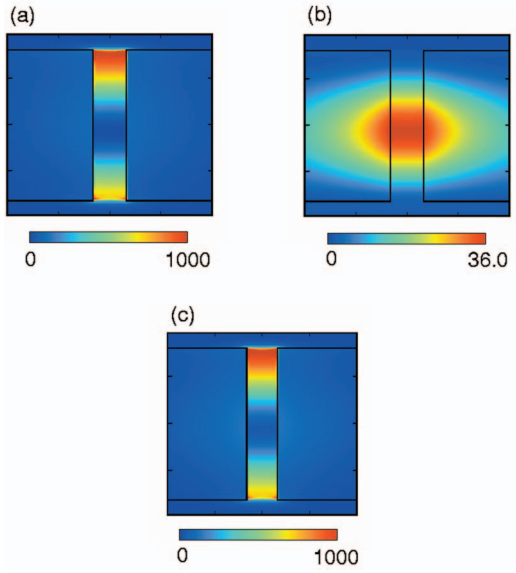


FIG. 12. (Color) The energy density distribution in the nanosheet plasmon cavity at the resonance of $m=1$. $T=3.3$ nm, $L=65$ nm, and $\lambda=970$ nm. (a) The electric, (b) the magnetic, and (c) the total-energy density. The outlines of the Au claddings are drawn for reference.

$$V_{mod} = \frac{\int_S u(\mathbf{r})d\mathbf{r}}{u_{max}} \times W, \tag{21}$$

where $u_{max}$ is the maximum energy density. In this study, we regarded the maximum energy density on the $z$ axis as $u_{max}$, since the true maximum but singular value at the corner of the metal claddings leads to an unrealistically small $V_{mod}$. In our cavity, the energy leaks out in the $xz$ plane. However, $V_{mod}$ of a leaky structure, similar to our system, has also been discussed.[49] We obtained the summation of the energy confined in our cavity as follows. It would be rational that the leaked energy into the free space is expressed by the summation of the localized energy, which exponentially decays in the normal direction, and the dissipated propagation energy. According to Appendix B, the localized energy in free space can be determined from the relationship between the distance from the cavity surface and the energy inside the surrounded area. In the system for $T=3.3$ nm and $L=65$ nm shown in Fig. 12, the ratio between the localized energy in free space, Au, and $SiO_2$ is 4.7: 6.3: 5.1. The energy is evenly localized in the three areas. The energy density in $SiO_2$ looks dominant in Fig. 12. However, a comparable amount of the energy is also stored in the Au and free space as a whole because the low-energy density is extensively distributed in these areas. From Eq. (21), $V_{mod}=0.0010$ $\mu m^3=0.0011\lambda^3=1.6TLW$.[50] As just described, $V_{mod}$ of our cavity is less than twice as large as volume of the core ($TLW$). While the quality factor ($Q$) of our cavity is not large, $V_{mod}$ can be small. Consequently, $Q/V_{mod}$ of our cavity can be comparable with that of conventional optical cavities.

### E. Validity and limitation of macroscopic electromagnetics

In this study, the breakdown of the theory based on a bulk dielectric function was not found even for 3-nm-thick core,

with respect to the relationship between the size of the cavity and the resonance wavelength. However, it does not mean that the consideration of other effects on the dielectric function is unnecessary. First, the effect of electron scattering at surfaces is not negligible because $L$ is as short as the mean free path of electrons in Au (~42 nm) for smaller $T$. In addition, when $k$ is greater than $\omega/\nu_F$ ($\nu_F$ is Fermi velocity, $1.4\times10^6$ m/s for Au;[51] $\omega/\nu_F=2713$ $\mu m^{-1}$ at $\omega=2.5$ eV), electron-electron interaction becomes strong.[52] In this study, the propagating modes themselves are not affected, because the dispersion relation of the MIM waveguide turns at a much smaller $k$ (maximum $k$ is 736 $\mu m^{-1}$ for $T=1$ nm). However, $k$ larger than $\omega/\nu_F$ might be present around the corners where the field exhibits singular behavior. These effects lead to the higher energy loss, i.e., cutdown of the $Q$ value and the field enhancement. Dips, which cannot be found in the calculated results, are observed in the experimental reflection spectra, especially for $T=3.3$ nm. It might be an indication of such additional energy loss. Scattering of plasmons by undulation of $SiO_2$ films could have influenced as well. When the core becomes much thinner, the electron distribution on both metal surfaces would overlap.[33,34] This also restricts attainable field enhancement.

## V. CONCLUSION

A structure has been proposed to realize a plasmon cavity with a nm-sized gap. The mode volume of this cavity can be small because the electromagnetic field is confined in the gap. Since the core in our cavity is filled with a dielectric, a molecule can be placed at the maximum field point. Consequently, this cavity exhibits good potential for enhanced Raman-scattering applications. However, the field enhancement was found to be only $10^3$. This leads to only moderate Raman enhancement. To realize higher Raman enhancement, we are planning to add improvements to the proposed structure.

Recently, similar structures were reported independently.[53,54] However, the interest of Ref. 53 lies in the negative refractive index for a different incident direction and polarization. The TM guided modes were not investigated there. Reference 54 also presents investigations on the response for the TE polarization.

Finally, we would like to point out that the resonance introduced in this study is applicable to any frequency domain (such as microwave and terahertz wave), if a material with a negative dielectric constant is used for the claddings.[28,35]

## ACKNOWLEDGMENTS

We are grateful to H. Miyazaki, J. Inoue, T. Ochiai, K. Ohtaka, H. Tamaru, K. Miyano, and T. Baba for discussion, and the Materials Analysis Station of the National Institute for Materials Science and N. Ishikawa for technical support. This work was supported by PRESTO of the Japan Science and Technology Agency and by the Ministry of Education, Culture, Sports, Science and Technology.

## APPENDIX A: EFFECT OF THE CORNER

In the calculation based on continuous media, it is difficult to treat a sharp corner of the metal. Such a calculation indicates a very high electric field localized in a nonphysically small area around the corner. Therefore we have rounded off the corners by a curvature of $R_c=0.25$ nm as Ref. 45. Here, the relation of the reflection spectra and the field enhancement to $R_c$ is discussed; $R_c$ was predefined as 0, 0.15, 0.25, and 0.50 nm. $R_c=0.15$ nm is almost as large as the atomic radius of Au (0.144 nm). Figure 13(a) is the reflection spectra. It is found that the magnitude of $R_c$ does not significantly affect the reflection spectra. However, a slight change is found in the field-enhancement spectra at the center of the core entrance [Fig. 13(b)]. When $R_c$ becomes larger, the field enhancement decreases and the resonance wavelength shifts to shorter λ. While the difference for $R_c=0.50$ nm can not be ignored, that for $R_c=0.25$ nm can be accepted. The relative error of the field is 4%. Calculation convergence is slow for much smaller $R_c$. However, the calculation results do not change significantly. Therefore we judged that the employment of a curvature of $R_c=0.25$ nm is reasonable.

## APPENDIX B: ENERGY IN THE FREE SPACE

The energy leakage from a cylindrical scatterer is considered for simplicity. The energy density $u(\rho)$ around the cylinder can be expressed by

$$u(\rho) = \alpha \exp\left(-\frac{\rho}{\tau}\right) + \frac{\beta}{\rho}, \tag{B1}$$

where $\rho$ is the distance from the center of the cylinder, and $\alpha$ and $\beta$ are constants. The first term of Eq. (B1) is the localized energy, and the second term indicates transmission of a constant power in the 2D space. Here, the energy $U_{free}$, which exists from the scatterer surface $\rho=P$ to $P+\Delta P$, is described as

$$U_{free} = \int_P^{P+\Delta P} [u(\rho)] 2\pi\rho d\rho$$

$$= A - A\exp(-B\xi) + C\xi\exp(-B\xi) + D\xi, \tag{B2}$$

where $\Delta P/P=\xi$ is the normalized distance from the surface

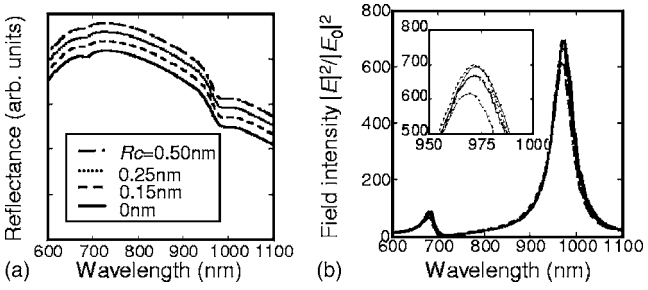


FIG. 13. Effects of the radius at the corners. $T=3.3$ nm and $L=65$ nm. $R_c=0$, 0.15, 0.25, and 0.50 nm. (a) The reflection spectra. Each spectrum is offset. (b) The field intensity enhancement spectra. The inset shows the details around the peak. Spectra are not offset in (b).

of the scatterer, and $A$, $B$, $C$, and $D$ are constants. When the integrated energy around the nanosheet plasmon cavity is calculated as a function of $\xi$, it actually agreed well with the form of Eq. (B2). Thus the integrated energy was fitted to Eq. (B2). The first three terms of Eq. (B2) show the localized component of $U_{free}$, and the fourth term represents the propagating component. The localized component of $U_{free}$ converges to $A$ for $\xi \to \infty$. Therefore $A$ obtained from the fitting to Eq. (B2) was regarded as the energy localized in the free space.

*Electronic address: KUROKAWA.Yoichi@nims.go.jp


[1] W. L. Barnes, A. Dereux, and T. W. Ebbesen, Nature (London) **424**, 824 (2003).
[2] J. Pendry, Science **285**, 1687 (1999).
[3] M. Fleischman, P. J. Hendra, and A. J. McQuillan, Chem. Phys. Lett. **26**, 163 (1974).
[4] T. W. Ebbesen, H. J. Lezec, H. F. Ghaemi, T. Thio, and P. A. Wolff, Nature (London) **391**, 667 (1998).
[5] H. A. Atwater, S. Maier, A. Polman, J. A. Dionne, and L. Sweatlock, MRS Bull. **30**, 385 (2005).
[6] J. B. Pendry, A. J. Holden, W. J. Stewart, and I. Youngs, Phys. Rev. Lett. **76**, 4773 (1996).
[7] H. Xu, E. J. Bjerneld, M. Käll, and L. Börjesson, Phys. Rev. Lett. **83**, 4357 (1999).
[8] O. Inoue and K. Ohtaka, J. Phys. Soc. Jpn. **52**, 3853 (1983).
[9] H. Xu, J. Aizpurua, M. Käll, and P. Apell, Phys. Rev. E **62**, 4318 (2000).
[10] M. Futamata, Y. Maruyama, and M. Ishikawa, J. Phys. Chem. B **107**, 7607 (2003).
[11] K. Li, M. I. Stockman, and D. J. Bergman, Phys. Rev. Lett. **91**, 227402 (2003).
[12] E. Hao and G. C. Schatz, J. Chem. Phys. **120**, 357 (2004).
[13] H. Tamaru, H. Kuwata, H. T. Miyazaki, and K. Miyano, Appl. Phys. Lett. **80**, 1826 (2002).
[14] W. Rechberger, A. Hohenau, A. Leitner, J. R. Krenn, B. Lamprecht, and F. R. Aussenegg, Opt. Commun. **220**, 137 (2003).
[15] D. P. Fromm, A. Sundaramurthy, P. J. Schuck, G. Kino, and W. E. Moerner, Nano Lett. **4**, 957 (2004).
[16] T. Atay, J. H. Song, and A. V. Nurmikko, Nano Lett. **4**, 1627 (2004).
[17] L. Gunnarsson, T. Rindzevicius, J. Prikulis, B. Kasemo, M. Käll, S. Zou, and G. C. Schatz, J. Phys. Chem. B **109**, 1079 (2005).
[18] P. Mühlschlegel, H.-J. Eisler, O. J. F. Martin, B. Hecht, and D. W. Pohl, Science **308**, 1607 (2005).
[19] H. T. Miyazaki and Y. Kurokawa, Phys. Rev. Lett. **96**, 097401 (2006).
[20] R. Zia, M. D. Selker, P. B. Catrysse, and M. L. Brongersma, J. Opt. Soc. Am. A **21**, 2442 (2004).
[21] J. A. Porto, F. J. Garcia-Vidal, and J. B. Pendry, Phys. Rev. Lett. **83**, 2845 (1999).
[22] S. Astilean, P. Lalanne, and M. Palamaru, Opt. Commun. **175**, 265 (2000).
[23] H. E. Went, A. P. Hibbins, J. R. Sambles, C. R. Lawrence, and A. P. Crick, Appl. Phys. Lett. **77**, 2789 (2000).
[24] Y. Takakura, Phys. Rev. Lett. **86**, 5601 (2001).
[25] F. Yang and J. R. Sambles, Phys. Rev. Lett. **89**, 063901 (2002).
[26] J. Bravo-Abad, L. Martin-Moreno, and F. J. Garcia-Vidal, Phys. Rev. E **69**, 026601 (2004).
[27] J. Lindberg, K. Lindfors, T. Setala, M. Kaivola, and A. T. Friberg, Opt. Express **12**, 623 (2004).
[28] J. Takahara and T. Kobayashi, Opt. Photonics News **15**, 54 (2004).
[29] G. J. Kovacs and G. D. Scott, Phys. Rev. B **16**, 1297 (1977).
[30] S. C. Kitson, W. L. Barnes, and J. R. Sambles, J. Appl. Phys. **84**, 2399 (1998).
[31] J. Vuckovic, M. Loncar, and A. Scherer, IEEE J. Quantum Electron. **36**, 1131 (2000).
[32] J. Takahara, Y. Fukasawa, and T. Kobayashi, J. Korean Phys. Soc. **47**, 43 (2005).
[33] J. Lambe and S. L. McCarthy, Phys. Rev. Lett. **37**, 923 (1976).
[34] S. Ushioda, J. E. Rutledge, and R. M. Pierce, Phys. Rev. Lett. **54**, 224 (1985).
[35] E. N. Economou, Phys. Rev. **182**, 539 (1969).
[36] T. Takano and J. Hamasaki, IEEE J. Quantum Electron. **8**, 206 (1972).
[37] J. A. Dionne, L. A. Sweatlock, H. A. Atwater, and A. Polman, Phys. Rev. B **73**, 035407 (2006).
[38] G. I. Stegeman, R. F. Wallis, and A. A. Maradudin, Opt. Lett. **8**, 386 (1983).
[39] P. B. Johnson and R. W. Christy, Phys. Rev. B **6**, 4370 (1972).
[40] In Figs. 1 and 5 of Ref. 19, turns of the dispersion relations were not found because we used only the real part of the dielectric function of Au for the calculation of the dispersion. We revised this point in this paper. There is no difference except for the presence of this turning point.
[41] J. A. Dionne, L. A. Sweatlock, H. A. Atwater, and A. Polman, Phys. Rev. B **72**, 075405 (2005).
[42] I. Gontijo, M. Boroditsky, E. Yablonovitch, S. Keller, U. K. Mishra, and S. P. DenBaars, Phys. Rev. B **60**, 11564 (1999).
[43] L. D. Landau, E. M. Lifshitz, and L. P. Pitaevskii, *Electrodynamics of Continuous Media*, 2nd ed. (Butterworth-Heinemann, Oxford, 1984).
[44] C. A. Brebbia, J. C. Telles, and L. C. Wrobel, *Boundary Element Techniques* (Springer, Berlin, 1984).
[45] J. P. Kottmann, O. J. F. Martin, D. R. Smith, and S. Schultz, Phys. Rev. B **64**, 235402 (2001).
[46] J. M. Steele, C. E. Moran, A. Lee, C. M. Aguirre, and N. J. Halas, Phys. Rev. B **68**, 205103 (2003).
[47] G. Schider, J. R. Krenn, A. Hohenau, H. Ditlbacher, A. Leitner, F. R. Aussenegg, W. L. Schaich, I. Puscasu, B. Monacelli, and G. Boreman, Phys. Rev. B **68**, 155427 (2003).
[48] J. S. Foresi, P. R. Villeneuve, J. Ferrera, E. R. Thoen, G. Steinmeyer, S. Fan, J. D. Joannopoulos, L. C. Kimerling, H. I. Smith, and E. P. Ippen, Nature (London) **390**, 143 (1997).
[49] O. Painter, R. K. Lee, A. Scherer, A. Yariv, J. D. O'Brien, P. D. Dapkus, and I. Kim, Science **284**, 1819 (1999).
[50] $V_{mod}=0.000\,95\ \mu m^3=0.0012\lambda^3=1.6TLW$ in Ref. 19 is obtained for $T=3.3$ nm and $L=59$ nm, our minimum fabricated cavity.
[51] C. Kittel, *Introduction to Solid State Physics* (John Wiley & Sons, New York, 1953).

[52] I. A. Larkin, M. I. Stockman, M. Achermann, and V. I. Klimov, Phys. Rev. B **69**, 121403(R) (2004).
[53] V. M. Shalaev, W. Cai, U. K. Chettiar, H. K. Yuan, A. K. Sarychev, V. P. Drachev, and A. V. Kildishev, Opt. Lett. **30**, 3356 (2005).
[54] K. H. Su, Q. H. Wei, and X. Zhang, Appl. Phys. Lett. **88**, 063118 (2006).